Dynamic EO/IR Satellite Signature Prediction with High-Fidelity MuSES Simulation

Corey D. Packard[a], **Casey D. Demars**[b], **Logan R. Canull**[a], **David W. Tyler**[b,c], **Christopher Rodgers**[b], **Zachary J. Edel**[a], **and Timofey Golubev**[a]
[a]*ThermoAnalytics, Inc.*
[b]*The Tech7 Company*
[c]*The University of Arizona College of Optical Sciences*

ABSTRACT

Space-domain awareness (SDA) via remote thermal imaging has benefits over conventional visible and SWIR imaging, potentially providing insight into the operational state of observed satellites. LWIR sensors provide capability for daytime and nighttime imaging, as demonstrated with the 3.6 meter telescope at the AMOS site on Maui, Hawaii. Satellite-to-satellite imaging using an LWIR sensor has been demonstrated in GEO with Mission Extension Vehicle-2 (MEV-2) capturing imagery of Intelsat 901 on approach for docking. In order to understand the capability that thermal dominant bands such as MWIR and LWIR play in SDA, a robust simulation capability must be developed to evaluate these phenomena.

The computational complexity required for radiative transfer simulation has previously resulted in a lag in the progress of satellite-focused thermal modeling in comparison to similar tools developed for visible and SWIR sensors. In this work, we demonstrate the ability of MuSES to predict both internal and external temperature distributions for 3D satellite models. MuSES uses orbital boundary conditions to simulate transient solar loading, thermal radiation to space and from Earth, as well as conductive and radiative heat transfer from internal components such as electronics. Additionally, solar panel efficiency and battery cell charge/discharge cycling can be realistically incorporated via the coupled thermal/electrical multi-physics solvers in MuSES. Surface facets are attributed with spectral optical surface properties to generate radiance maps via BRDF-based ray tracing of the 3D temperature distributions. This allows radiometric signal levels and contrast metrics to be generated using sensor simulations for both ground- and space-based imaging platforms. This requires combining the predicted band-integrated spectral radiance of the satellite with the appropriate background radiance (i.e., sky radiance for Earth-based observations) and estimates of shot noise fluctuations based on integration time.

The output of this process is a useful indication of the signal-to-noise ratio expected for the corresponding sensor model and provides a means to compare sensor design parameters. Using these tools, we demonstrate how solar panel efficiency and internal heat sources can impact surface temperature distributions and infrared signal levels during observations of satellites in LEO and GEO. Comparisons are made between Earth-based and space-based (satellite-to-satellite) observations. Additionally, the significance of solar panel efficiency (which varies with module temperature and solar incidence angle, and is zero for inoperable satellites) on radiometric signature is explored.

1. INTRODUCTION

As the proliferation of satellites and space debris continues, and with the increasing militarization of space, enhancing the detection, tracking, identification, and characterization of space objects has become crucial. Limitations such as sky background and clutter must be overcome for continuous (24/7) space surveillance to be as effective as possible. While short-wave sensors, electro-optical telescopes, and space surveillance radars are indispensable, each has inherent limitations. This underscores the need for complementary sensor technologies to bridge these gaps. Furthermore, satellite characterization – understanding the mission, material composition, capabilities, vulnerabilities, attitude and operational state of an orbiting object – demands multiple approaches.

Ascertaining the operational state of a satellite is a sensor mission particularly well-suited to long-wave infrared (LWIR) measurements, since radiance values in that waveband are typically dominated by physical temperatures. As an example, it was proposed to estimate surface temperatures from spatially resolved data from LWIR data [21]. This could in turn be used to estimate internal power generation levels, from which inferences can be drawn about the satellite's payload and mission. If the rate of cooling can be estimated from measured data (e.g., during an eclipse), inferences might be made about thermal mass, material composition, vulnerability to directed energy or kinetic weapons, or payload age. Furthermore, LWIR sensing can effectively extend short-wave surveillance capabilities past the relatively short "terminator" periods when the satellite is illuminated by the Sun against a dark sky. Thermal infrared wavebands, dominated by physical temperature emissions (and reflections), can be employed to obtain satellite signatures when no solar-reflections are present for short-wave observation. Finally, time-sampled temperature measurements – thermal light curves, essentially – could likely be used to estimate satellite pose given enough supporting information.

Several initiatives employing LWIR data for space-domain awareness (SDA) characterization have utilized the 3.6-meter Advanced Electro-Optical System (AEOS) telescope on Maui, Hawaii. Hall *et al.* (2006) [8] conducted observations of NASA's *Image* satellite using the Haleakala-based AEOS LWIR imager to diagnose the operational status of that satellite after all communications with the satellite were lost. Due to small temperature differences observed when the satellite was in standby mode or fully operational, the authors were not able to make a confident conclusion regarding the satellite's operational state based solely on the LWIR light curve. In a subsequent study, Hall *et al.* (2015) [9] conducted a controlled experiment with the Naval Research Laboratory satellite *SpinSat* to evaluate the effectiveness of detection Electrically-Controlled Solid Propellant (ESP) thruster firing using LWIR light curves. Werth *et al.* [22] exploited the relatively low levels of turbulence-induced blurring at LWIR wavelengths to decrease multi-frame blind deconvolution (MFBD) processing times and improve image reconstruction quality by fusing the LWIR-based object support constraint with the visible-wavelength data.

Satellite characterization falls within a broader category of mathematical inverse problems, which are often ill-posed, with multiple solutions fitting the data and no definitive analytical solution. In lieu of viable formal solutions, forward predictions made by physics-based simulations using a high-fidelity simulation model can be compared with measurements. Various approaches for thermal modeling and analysis of spacecraft have been demonstrated including analytical models [6] and specialized software packages [4, 10]. In general, thermal analysis is leveraged for satellite thermal control design to assess the likelihood that satellite components will withstand the extreme hot and cold conditions experienced in space [1, 5]. These approaches, while useful for evaluating satellite thermal control strategies, often do not provide the high-fidelity temporal dynamics required for accurate system-level thermal light curves to be exploited for SDA characterization.

The SDA community has expended significant resources understanding how to exploit both imaging and non-imaging short-wave measurements - in visible and SWIR wavebands - with some notable successes. Moreover, several efforts have attempted to exploit polarimetry and spectroscopy for SDA applictions [2, 18, 19, 23]. However, the thermal regime (and particularly LWIR) has remained relatively underutilized due to the limited sensitivity of thermal infrared sensors and a lack of efficient and practical tools for understanding satellite thermal dynamics. The focus of this current effort, presented by ThermoAnalytics and Tech7, looks to exploit both resolved and unresolved infrared sensing (particularly LWIR 8-12μm, but also MWIR 3-5μm), building on the progress we reported previously [3]. This is done by demonstrating a state-of-the-art modeling and simulation approach designed to incorporate available thermal infrared data. For both low earth orbit (LEO) and geosynchronous orbit (GEO) scenarios, we employ MuSES™ to predict the dynamic temperatures of a communications satellite throughout its orbit, in two operational states.

In this paper, we demonstrate a high-fidelity approach for simulating dynamic thermal signatures of resident space objects (RSOs) using the validated [13] commercial software MuSES™. In Section 2 we describe MuSES and detail its capability to simulate accurate thermal signatures of RSOs over various orbital regimes and for different operating conditions. We include an explanation of the coupled thermal-electrical simulation methodology that serves as a foundation for predicting surface temperatures and generated EO/IR radiance images from the perspective of a virtual sensor. Section 3 details the communications satellite that served as the focus of this study, and describes the operating conditions of the simulated RSOs. We describe different orbital scenarios, including a LEO and a GEO, that were used for this signature investigation. In Section 4 we present a variety of results including coupled thermal-electrical simulation predictions, subsequent dynamic signatures (including but not limited to LWIR), and relevant supporting sensor images. We present a summary of our findings for this representative communications satellite in Section 5, and share our conclusions from this work.

2. MuSES

MuSES™ (Multi-Service Electro-Optic Signature) is an export-controlled commercially-available thermal and EO/IR sensor radiance prediction software developed by ThermoAnalytics that uses a numerical, finite volume method based on first principles physics to solve energy balance for heat transfer due to radiation, conduction, and convection. MuSES is considered the gold-standard for high-fidelity U.S. Army ground vehicle simulation (especially for determining compliance with signature requirements and evaluating low-observable technologies) and is used by domestic and ally defense agencies to predict the signature of high-value tracked and wheeled vehicles, maritime vessels, human personnel, manned and autonomous rotary and fixed-wing aircraft. The thermal-only version of MuSES (referred to as TAITherm™) is used by many major automotive OEMs around the world, as well as in other industries like architecture, aerospace, manufacturing and textiles. MuSES has been validated [12, 17] under contract for US Army, US Navy and Department of Energy applications, and several DoD groups accept MuSES prediction results as a method for demonstrating signature management (SIGMAN) compliance against EO/IR signature requirements. Past examples of this include DDG 1000 (2005), Future Combat Systems (FCS, 2004-2007), Joint Light Tactical Vehicle (JLTV, 2008-2016) and the XM30 Mechanized Infantry Combat Vehicle (formerly known as the Optionally Manned Fighting Vehicle, 2022-present). MuSES is used by all DoD agencies, several National Labs, the intelligence community and many US Department of State-approved foreign groups.

Thermal simulation with MuSES requires a 3D surface mesh (and volume mesh, where desired) to describe the system geometry. Automatic view factor calculation (determining which elements radiate to other elements) as well as lateral and vertical conduction (across the surface and through the thickness of a surface, respectively) are handled via the nodal network automatically generated from the surface mesh. This provides an efficient means of calculating radiative, conductive (and convective, when applicable) heat transfer. An example of the communication satellite geometry used for this effort is shown in Figure 1. The thickness of each surface is handled virtually by a user-supplied thickness that allows analysts to study the impact of surface thickness without needing to regenerate the 3D mesh. Element-to-element and/or part-to-part thermal links can be used to define conduction paths other than those present in the meshed nodal network. Thermal material properties from a provided database are applied to each component to characterize the transient thermal response to orbital boundary conditions and mission profiles. Optical properties (e.g., albedo and thermal emissivity) are specified for each surface to govern radiation exchange; internal heat sources (see Figure 2) can also be defined with varying levels of sophistication depending on user requirements and available information. Physical temperatures are calculated for all elements at each discrete timestep in the transient simulation using these model attributes and dynamic boundary conditions.

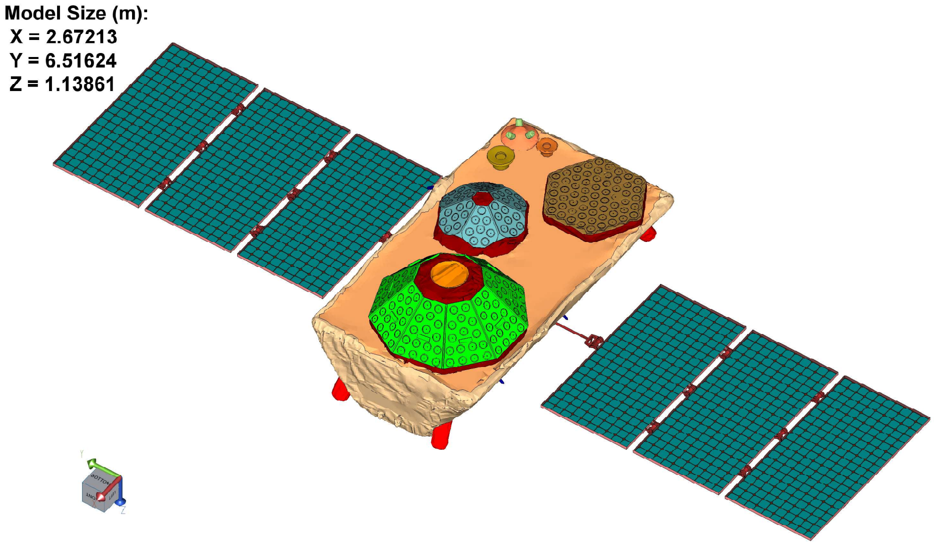

Fig. 1: Globalstar satellite geometry shown in MuSES, with part/feature edges shown but with the element mesh suppressed for visual clarity. The different colors correspond to distinct parts in the simulation model (e.g., PV panels, antennas, MLI).

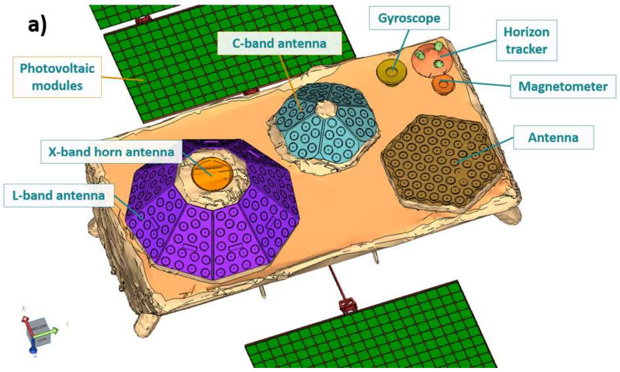

Fig. 2: Globalstar satellite geometry shown in MuSES with various parts labeled, including external and internal components (left and right, respectively).

These (orbital) boundary conditions can be calculated by the MuSES software, supplied by the user or a combination of these two approaches. Taking a LEO path as an example, MuSES can be supplied (by a variety of orbital tools) with a variety of orbital and environmental parameters based on a TLE (two-line element) set. These include Earth-centered Earth-fixed (ECEF) satellite positions which specify X-Y-Z location relative to the Earth and Sun, satellite attitude quaternions to control orientation with respect to the Earth, and solar angle (which is used to correctly position the Sun). Together, these boundary conditions are used to automatically position the satellite, Earth and Sun correctly with respect to each other for thermal simulation purposes. However, for a simpler GEO path and a non-tumbling payload, MuSES can calculate transient solar position, solar angles and eclipse times based on simple user inputs such as latitude, longitude and satellite altitude above the Earth. This multiplicity of approaches for supplying dynamic orbital boundary conditions provides flexibility and control to the analyst.

MuSES can incorporate batteries into thermal simulations via a coupled thermal/electrical multi-physics solution [14, 15, 16]. The current passing through each battery cell is dependent upon the electrical boundary conditions and the state of the cell, including the depth of discharge and temperature of the cell. The heat generated in a cell is modeled with both reversible (entropic heating) and irreversible (Joule heating) terms, and is dependent on the current through the cell and the temperature-dependent state of the cell. The thermal model uses these generated heat rates to calculate the evolution of the battery cell temperatures. This codependence, where current is temperature-dependent and heating is current-dependent, shows the benefits of a coupled thermal/electrical solution.

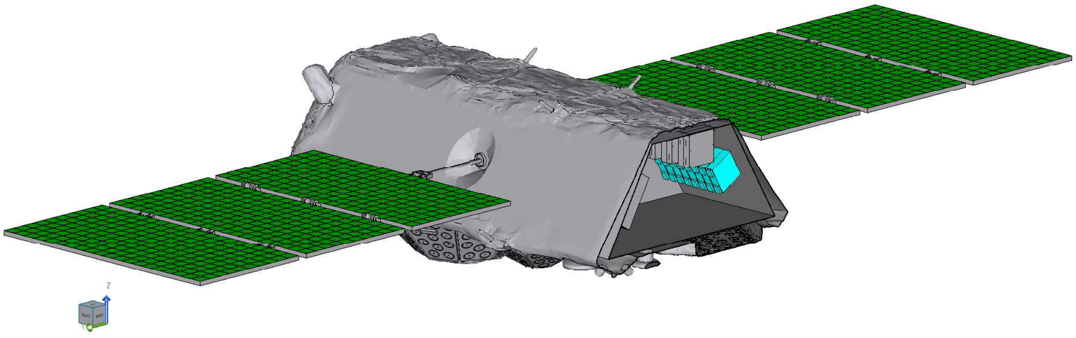

Fig. 3: Communications satellite with deployed solar panels (green) and internal battery cells (cyan) colored for clarity; interior parts are visible due to the cutaway view employed here. Various external and internal active components are powered by a combination of the PV system and battery pack, depending on sunlit/eclipse conditions.

MuSES is also capable of integrating photovoltaic (PV) panels into thermal simulations, again via a coupled thermal/electrical multi-physics solution [7]. The PV electrical calculations are performed at the conclusion of each discrete thermal simulation timestep, and photogenerated energy production is then calculated by one of two methods.

Figure 3 illustrates the incorporation of solar panels (whose efficiency is solar angle-dependent and temperature-dependent) and battery cells (which are charged by the PV panels and discharged by the active components).

The battery cells and solar panels can be represented several ways, depending on the information available to the simulation engineer and the fidelity required. One method is to use an equivalent circuit, as shown in Figure 4. As mentioned earlier, MuSES solves both the thermal and electrical problems concurrently due to inter-dependencies. This results in accurate predictions for PV efficiency and harvested solar energy, battery current/power/SoC (state of charge) information, as well as trustworthy temperature calculations for both of these subsystems (and all others, including active components). These physical temperatures serve as the necessary foundation for EO/IR sensor predictions in thermal wavebands (e.g., MWIR and LWIR), which we explore in this work.

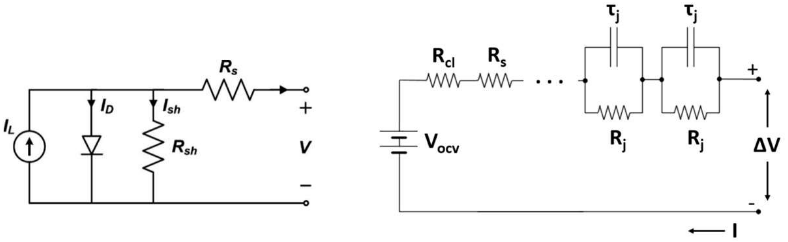

Fig. 4: These diagrams illustrate the equivalent circuit approaches for PV panels (left) and battery cells/packs (right) that can be employed by MuSES.

3. SCENARIOS

In this work, we explore different orbits and operating conditions to study the impacts they have on the thermal signature of a communications satellite. A general LEO has an altitude between 500 and 2000 kilometers moving between being sunlit and eclipsed by Earth's shadow. Shadowing in GEO also occurs around the solstices when the sun is aligned with the equatorial plane. Passing in and out of shadow changes the temperature of the satellite while impacting the incident solar radiation falling on the PV panels. When the solar panels are not sunlit and thus cannot collect solar radiation, any electronic loads that must be active during the eclipse must be powered via battery dissipation. These factors contribute to the overall distribution of temperatures across the satellite. We explore a LEO orbit and a GEO orbit, both of which experience one or more eclipses. During each orbit the satellite electronics are placed under different loads to study the impact of the communication electronics on the thermal infrared signature.

3.1 Description of the Communications Satellite

This work focuses on a communications satellite loosely based on the GlobalStar, so a brief description of the orbital payload of interest is appropriate here. The satellite has exterior dimensions of 2.67 m x 6.52 m x 1.14 m and is equipped with six large, deployed triple-junction GaAs PV panels (shown in Figure 5). Although MuSES is capable of incorporating rigged models with articulating solar panels, for this effort the PVs were fixed. In the GEO scenario each panel is double-sided, collecting solar energy from either the Earth-facing side or the surface facing away from the Earth. This design was selected to ensure adequate solar energy could be gathered throughout the GEO. Future satellite models will incorporate rigging to allow the rotation of solar panels to track the sun. Each panel has an active collecting surface area of 0.94 m^2 per side, totalling 11.28 m^2 (though only half of that can collect direct sunlight at any one time).

The solar panels have a solar absorptivity of 0.65 (which includes the nominal stated PV efficiency of 29%) and a thermal emissivity of 0.90. This is in contrast to the highly reflective MLI found covering much of the remaining satellite surfaces, which has a solar absorptivity of 0.25 and a very low thermal emissivity of 0.026. These values are used by MuSES for its dual-band radiation solver; EO/IR renderings employ spectral surface descriptions (i.e., wavelength-dependent emissivity, diffuse and specular reflectivity values) and the Sanford-Robertson BRDF model.

These solar panels harvest energy from the sun with a temperature-dependent and incident-angle dependent efficiency that is calculated during the dynamic simulation. This absorbed solar energy is used to charge the internal battery pack shown in Figure 3. Eight (8) battery cells, which together have a capacity of 54 A-hr, are used to power the internal electronics when sufficient solar energy is not present. A battery management system (BMS) is employed to enforce

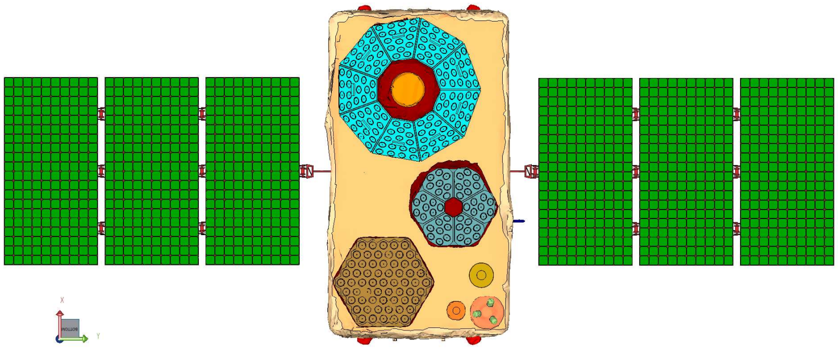

Fig. 5: Illustration of communications satellite from Earth's perspective with its six large PV panels deployed to gather solar energy and convert it to electrical power.

charge/discharge limits when the state-of-charge (SoC) is above 90% or below 10%, and an initial SoC of 50% is assumed. For the LEO scenario described later, the the total component power draw of the communications satellite varies throughout the orbit with an average of 467.4 W over the LEO period. The GEO scenario explored during this effort assumed a constant satellite power budget of 467.1 W over the orbital period. These power budgets describe the component load of the "ON" satellite model; for the "OFF" satellite, all components are inactive, drawing no power. This means that the battery is neither charging nor discharging, and the PV panel array does not generate any power since none is consumed by the deactivated satellite.

3.2 Scenario 1: Communications Satellite in LEO

The first scenario investigated during this effort is a LEO with its orbital path based on the two-line element for a SpaceX Starlink satellite, given as:

```
0 STARLINK-2461
1 48428U 21040A   22305.35754059  .00001394  00000-0  11247-3 0  9998
2 48428  53.0533 282.8707 0002250  51.9033 308.2159 15.06402681 83306.
```

The orbit was propagated using the Simplified General Perturbations (SGP4) model [20] starting at 2022-11-01T00:00:00 for 360 time samples with 60 second sampling. The orbital path is shown in Figure 6 (a) along with the eclipse periods shown in Figure 6 (b). The orbital positions were scaled such that the altitude of the communications satellite was a constant 732 km above the Earth, and a three-axis stabilized attitude was employed.

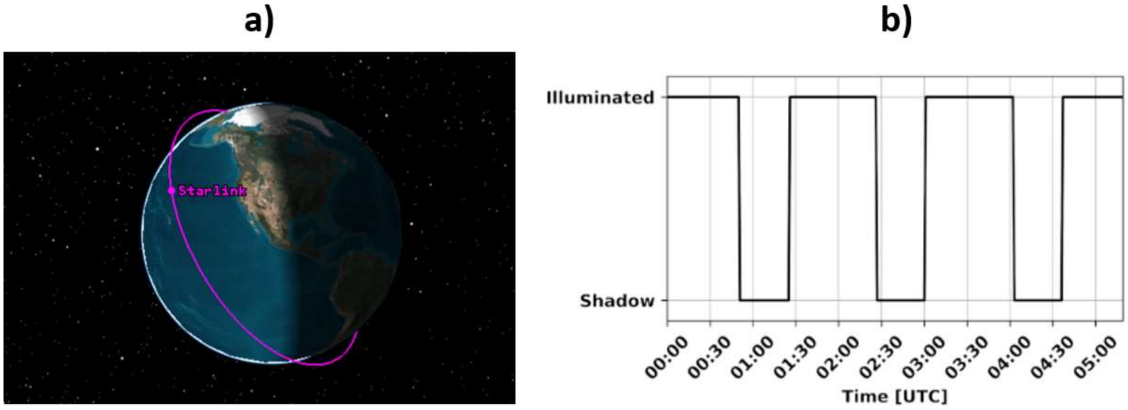

Fig. 6: (a) - Path of the Starlink-2461 orbit in the Earth-centered inertial coordinate frame, shown with Earth's terminator shadow. (b) - Status of object being illuminated or in shadow over the simulated time interval.

3.3 Scenario 2: Communications Satellite in GEO

The second scenario explored during this study is a geosynchronous orbit which placed the communications satellite at an altitude of 35,786 kilometers with its active communications components (e.g., antennas) directly facing the Earth. An equatorial orbit during eclipse season with a longitude of -136.96 degrees (i.e., 136.96 degrees West) was selected, using the GOES-17 TLE given as follows:

```
0 GOES 17
1 43226U 18022A   22241.66234375  .00000098  00000-0  00000-0 0  9994
2 43226   0.1013 278.8974 0000226 228.5100 291.5628  1.00272724 16507.
```

The orbit was propagated using SGP4 starting at 2022-09-18T00:00:00 for 3600 discrete timesteps with a 60 second temporal spacing, with the signature study focusing on the final 5.5 hours of that duration (e.g., 0630 to 1200 on 2022-09-20). The orbit is shown in Figure 7 (a) which illustrates that the satellite is in Earth's shadow. The eclipsed and sunlit periods are shown in Figure 7 (b); the eclipse period starts around 08:30 UTC and last slightly longer than one hour until just after 09:30 UTC.

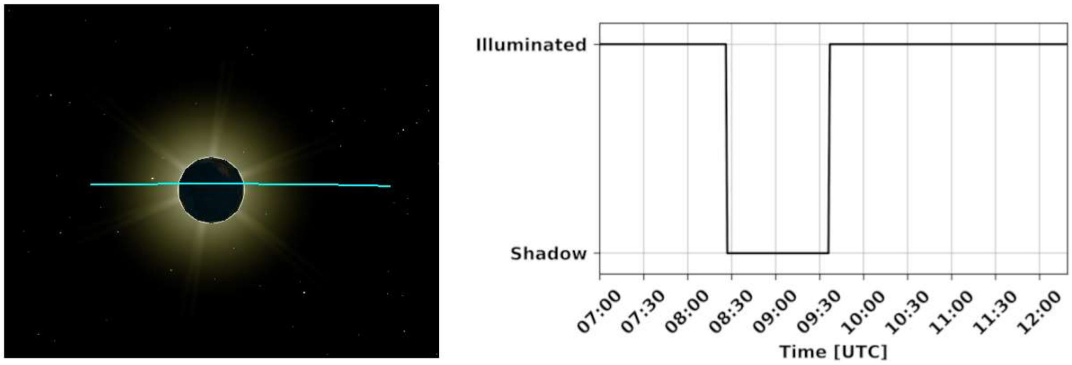

(a) (b)

Fig. 7: (a) Path of the GOES-17 Orbit in the Earth centered inertial coordinate frame with reference to the Earth and Sun. (b) Status of object being illuminated or in shadow over the simulated time interval of interest.

A three-axis stabilized attitude is again assumed, so the view factors from the various satellite surfaces to the Earth and space are constant. This means that only the solar illumination angle and altitude-dependent eclipse are time-dependent. MuSES calculates the dynamic solar position relative to the satellite geometry for the user-specified latitude and longitude, excluding solar loading entirely during the brief orbit segment when the object is eclipsed according to Figure 7 (b). For this scenario, the side of the satellite bus housing the external communications equipment (e.g., various antennas) faces the Earth, as can be seen in Figure 5 which shows the satellite from the Earth's perspective. In this scenario, the path of the sun relative to the satellite body reference frame in MuSES traces an arc that is primarily ”underneath” the satellite over the temporal period of interest. This results in the illumination of the Earth-facing side of the satellite, and this means that surfaces visible from Earth, shown in Figure 5, are primarily solar-illuminated for the final 5.5 hours, except for the eclipse, as shown in Figure 7 (b).

4. RESULTS

4.1 Results for Scenario 1: Communications Satellite in LEO

An orbit with an altitude of 732 km has a period of just over 99 minutes, so a 360 minute segment encompasses approximately 3.6 complete orbits around the Earth. The results of the thermal-electrical coupled MuSES simulation for the Starlink-based LEO scenario are portrayed in Figure 8. The six panels illustrate various related battery and PV panel quantities calculated by MuSES for the electronics “ON” case.

Panel a) indicates the average PV panel temperature, which oscillates during orbit as the solar cells traverse through sunlit and shadowed regions. The PV panel temperature is both a significant contributor to the signature of the satellite,

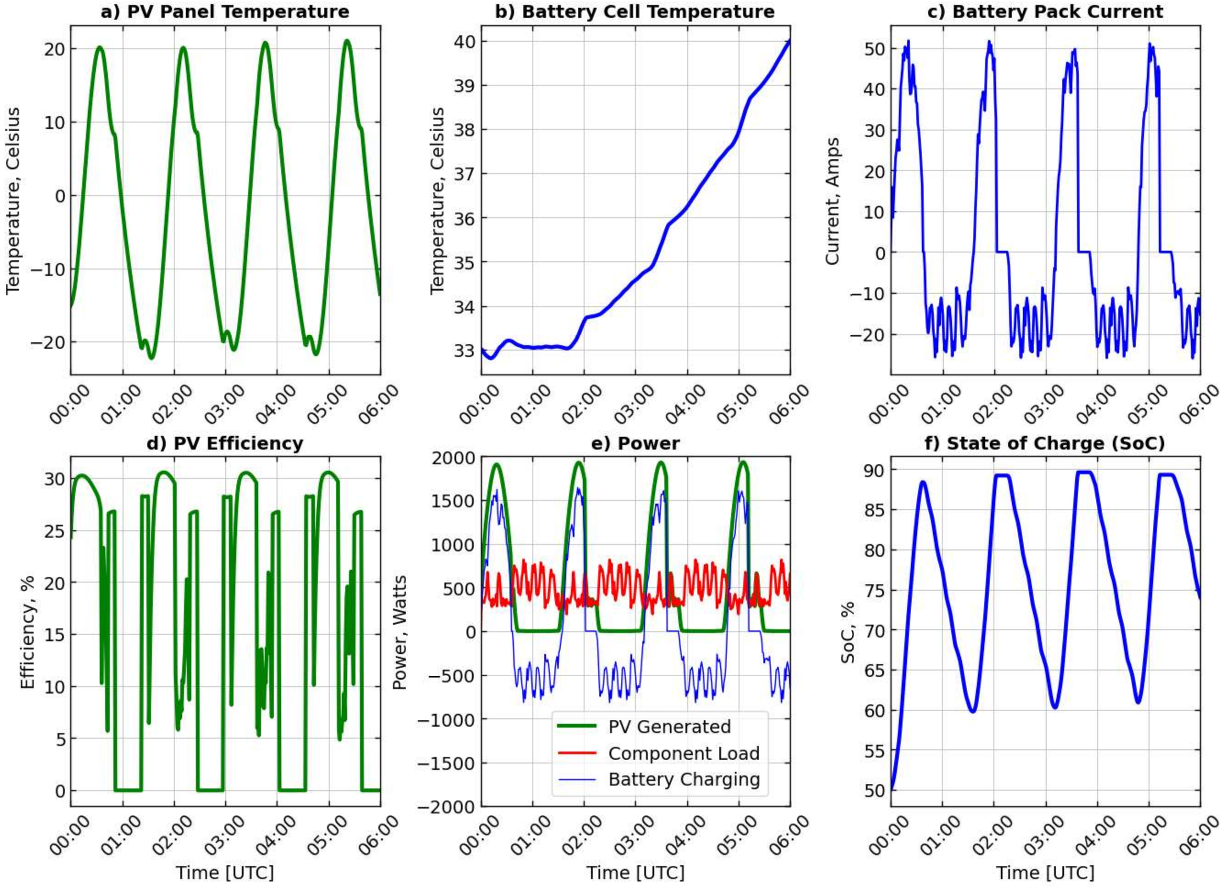

Fig. 8: Battery and PV panel results for a communications satellite in a LEO based on a Starlink TLE.

due to their physical size, and a contributing factor to the varying efficiency of the solar cells seen in Panel d). The average battery cell temperature, presented in Panel b), increases from its initial value during orbit due to the lack of thermal management in this simplified satellite design.

Panel e) depicts how the available PV power (shown in green) varies over several orbit periods, with several eclipse-induced outages evident when the "PV Generated" power goes to zero. Also shown is the variable system "Component Load", indicated in red, as it changes through the satellite mission. Note that if the battery is fully charged and no surplus power is needed from the PV array, the PV generated power is reduced to supply only what the component load requires. Finally, the blue plot illustrates the battery charging/discharging power (positive means charging, negative represents period of discharge). Taking these three power quantities together, we observe that during sunlit portion of the orbit the PV panels are able to power the components and charge the battery when necessary. During eclipses, the battery must supply the necessary electrical power to fulfill mission requirements.

Panel c) shows the battery pack current that results from the battery charging power curve in Panel e); again, positive values indicate time periods when the pack is being charged by surplus solar energy, and negative values depict when the battery must be discharged to power active components during an eclipse. Zero current values show when the battery is fully charged and the battery management system (BMS) disables charging. Panel f) shows the state-of-charge (SoC) of the battery pack, which begin orbiting charged to 50% of its total capacity and then ranges from fully charged (near 90% of total capacity) to 60% (during eclipses)

Beyond exterior and interior temperature predictions, MuSES was used to predict transient satellite hardbody signatures from the perspective of a virtual LWIR sensor viewing the orbiting payload from the perspective of another (chasing) LEO satellite on the same orbit but separated by a range of 5442 km. The results of this LWIR signature study, performed using a band-integrated 8-12 µm waveband, are shown in Figure 9 and Figure 10. In Figure 9 the transient LWIR average radiance of the two satellites are presented, depicting how the satellite with actively-powered components (whose “ON” signature is indicated with a thick red line) compares to the signature of the inactive satellite (indicated by a dotted black line, “OFF”). Figure 10 portrays well-resolved signature renderings for both the “ON” and “OFF” satellites for two specific orbit times, 0345 (sunlit) and 0430 (eclipsed). The PV panels are warmer for the “OFF” satellite due to its lack of solar energy conversion; since PV energy conversion decreases the effective solar absorptivity, the lack of energy conversion for the “OFF” satellite means more solar power is absorbed as heat and increases PV temperatures. The central satellite bus is slightly cooler for the inactive satellite (due to the lack of internal and external component heating) but the MLI blankets make this factor less significant than the very large, warmer solar cell array. Atmospheric extinction was excluded from these renderings as the slant path from the chasing LEO satellite to the satellite under observation was essentially outside the atmosphere.

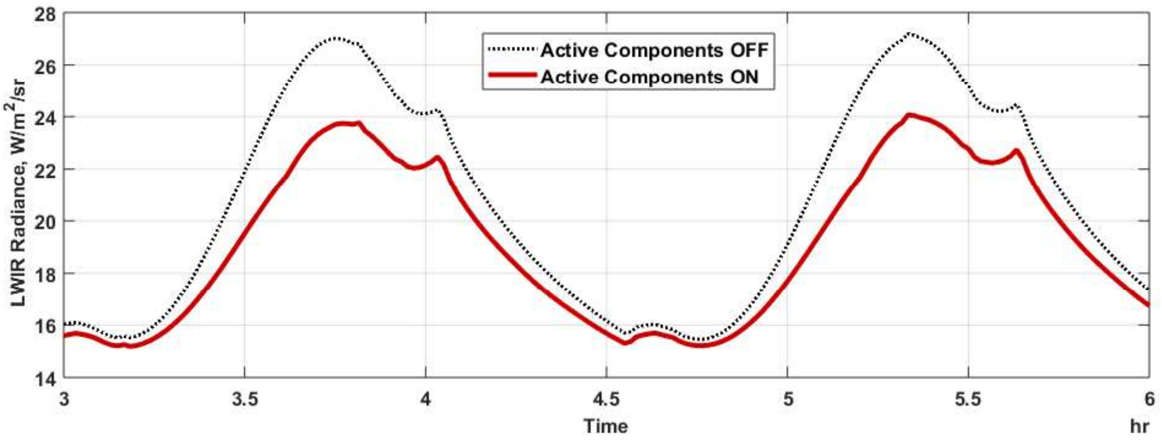

Fig. 9: LWIR results for a communications satellite in LEO where the average satellite signature, from a chasing LEO satellite’s perspective, is shown for two power states. The average transient LWIR radiance, computed from well-resolved virtual sensor images, is plotted as a function of orbit time for both power states. The thick, solid red line shows the spatially-averaged radiance of the active satellite (ON) and the dotted black line indicates the average satellite radiance when components are not being powered.

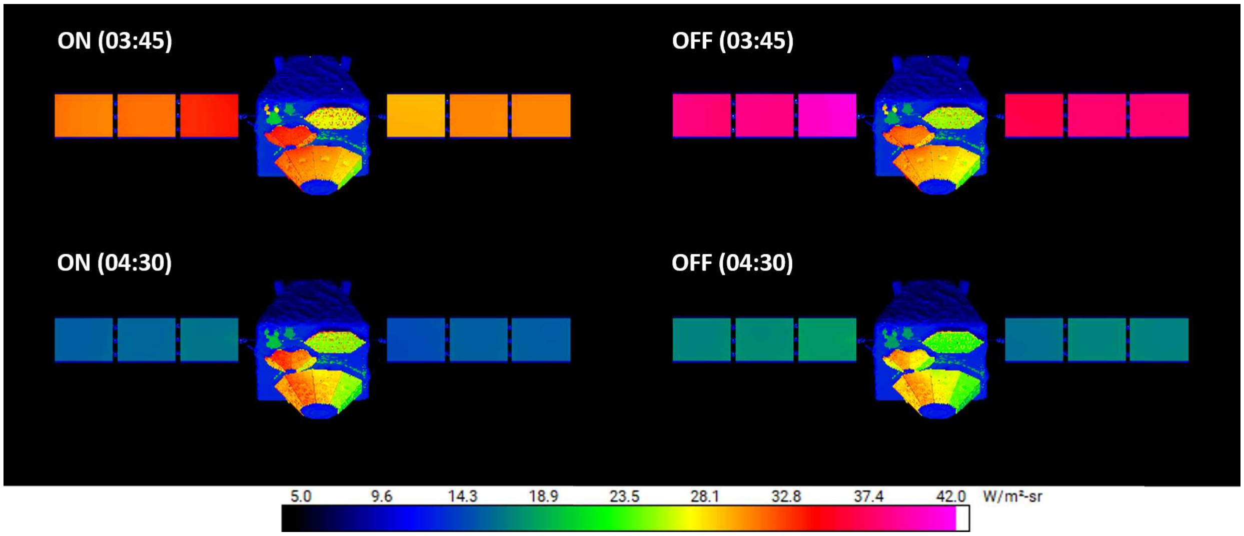

Fig. 10: LWIR sensor radiance renderings for a communications satellite in LEO. Two power states are shown, ON (left column) and OFF (right column). Additionally, two orbit positions are depicted, 03:45 (top row, which is during a sunlit region) and 04:30 (bottom row, which is an eclipsed orbit segment). These images indicate the perspective of the LEO sensor platform in fixed-range pursuit of the communications satellite.

In addition to the LWIR signature study performed on the LEO satellites, a MWIR investigation was also performed. The same LEO chasing scenario was considered, but this time with a 3-5 µm waveband sensor. The results of this exploration are shown in Figure 11, where the thick red line indicates the "ON" satellite transient signature and the black line and circular markers depict the "OFF" satellite. Again, average radiance tends to be greater for the inactive satellite due to the large, warmer PV panels. Both the "ON" and "OFF" satellite models exhibit average radiance spikes at various times. These signify times during the transient analysis where solar glints occur due to the geometric relationship between the Sun, the wrinkly and highly reflective MLI-covered satellite bus and the sensor being aligned just right. The specular lobe of the MLI blanket concentrates reflected solar energy into a relatively small solid angle, and this creates very large MWIR radiance values for a few sensor pixels resolving the satellite.

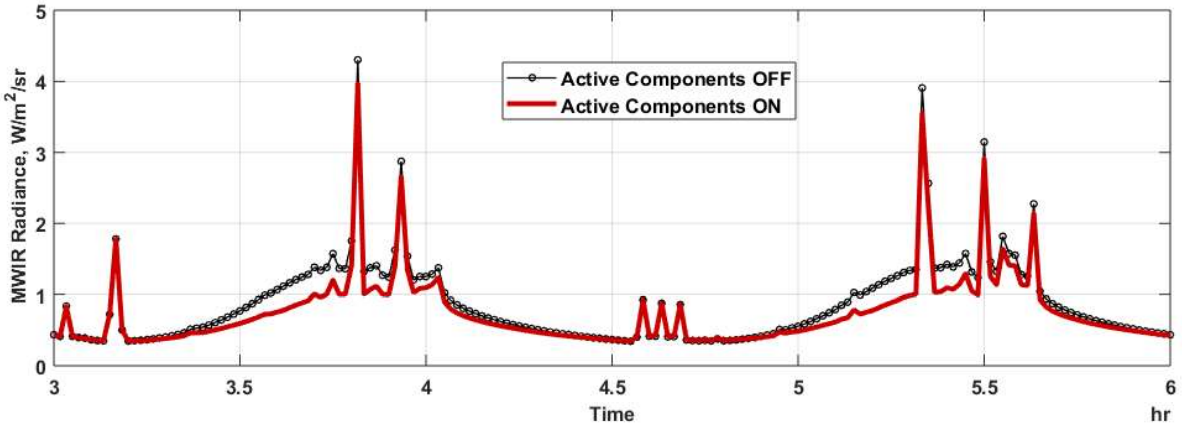

Fig. 11: MWIR results for a communications satellite in LEO where the average satellite signature, from a chasing LEO satellite's perspective, is shown for two power states.

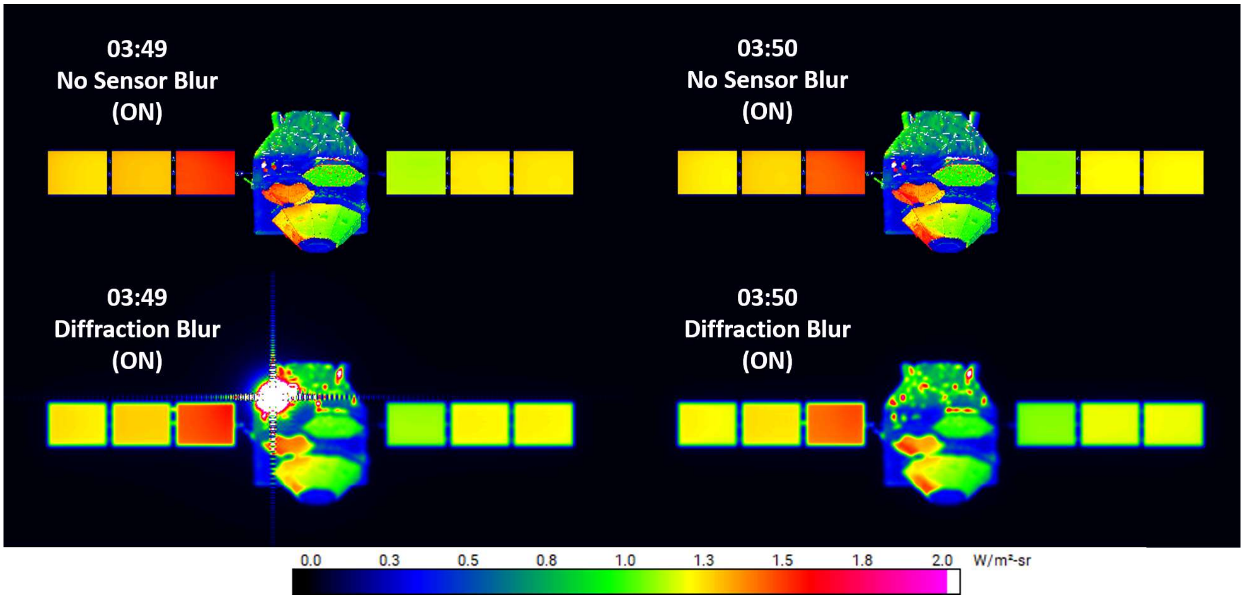

Fig. 12: MuSES-generated MWIR radiance images of the "ON" satellite at 03:49 and 03:50, both with and without sensor diffraction blur included. Solar glint reflecting off the specular MLI blanket occurs at 03:49, which results in very high MWIR radiance values for one or more sensor pixels depending on the inclusion or exclusion of sensor effects. Without diffraction blur, a very small number of pixels include glint, but the inclusion of diffraction-limiting sensor blur both reduces the maximum glint intensity and enlarged the glint-impacted area due to spatial averaging.

While the highly-resolved nature of the virtual sensor analysis performed for this study means a single pixel with an extremely high MWIR radiance can result from solar glints, Figure 12 demonstrates the effect that spatial averaging (in this case due to the inclusion of sensor diffraction blur) can have on solar glints. Note the impact of diffraction blur on the size (and severity) of solar glint in the MWIR imagery of Figure 12; without any blur the maximum pixel radiance is nearly 3400x greater due to glint, while the spatial averaging due to diffraction blur reduces this to 83x while increasing the number of glint-effected pixels. The number of pixels impact and the severity of the glint varies with image resolution and inclusion of pixel averaging, but the phenomenon itself is real and can be predicted by MuSES.

4.2 Results for Scenario 2: Communications Satellite in GEO

The thermal infrared results (e.g., LWIR) for the communications satellite in GEO are highly dependent on the surface temperature results, especially those on the Earth-facing side of the orbiting object. The temperatures of these critical surfaces are, in turn, highly influenced by variable solar loading during orbit. Figure 13 depicts the surface temperatures of several significant Earth-facing components including PV panels, MLI blanket and several antenna arrays. All of these surface temperatures rise during the sunlit portion (prior to 8:30), cool during the eclipse (approximately 08:30 to 09:30), then begin increasing again as the sun re-illuminates the Earth-facing side of the orbiting satellite. Note that the thermal management strategies of this satellite are simplified and were designed for LEO; this results in higher-than-desired temperatures during GEO, but the model was left unchanged.

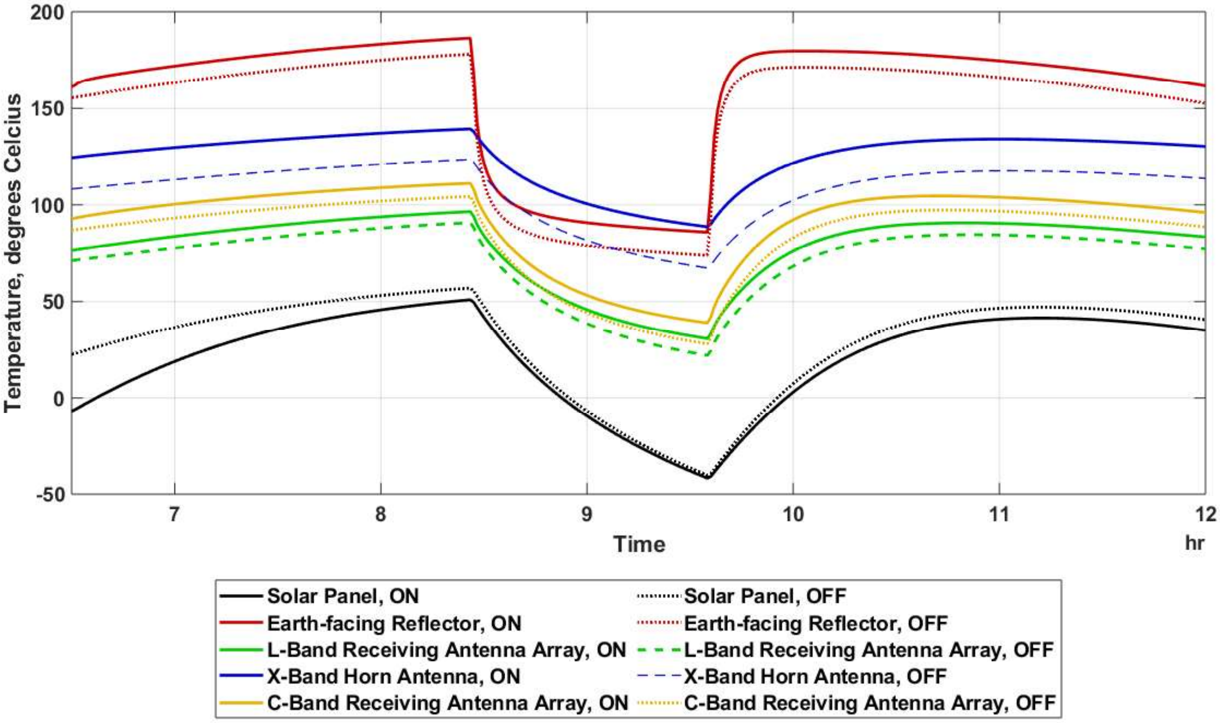

Fig. 13: Surface temperatures for important Earth-facing satellite components of the “ON” and “OFF” satellite models (solid vs. dotted/dashed, respectively). Note that for all components other than the PV panels, the surfaces of the “ON” satellite are warmer. Only the PV panels of the “ON” satellite are cooler than their “OFF” counterparts.

Due to the temperature-dominated nature of LWIR radiance, these same trends are observed in the pixel-averaged dynamic LWIR signature of the satellite (see the Figure 14, top). In the upper subplot, the black dotted line indicates the average satellite signature of the “OFF” satellite, as a function of time. The thicker red line represents the average dynamic signature of the orbiting “ON” satellite. During the sunlit orbit segment prior to the eclipse, the “OFF” satellite has a greater LWIR signature due to the warmer (inactive) PV panels. This follows from the temperatures seen in Figure 13 where for all components other than the PV panels, the surfaces of the “ON” satellite are hotter. Only the PV panels of the “ON” satellite are cooler than their “OFF” counterparts, but their physical size dominates a large percentage of the sensor field-of-view.

A transient VIS-band signature, computed with a flat-top response in the 525 to 725 nm waveband inspired by the Sloan R filter, is shown with open blue circles on a secondary Y-axis for reference. The wrinkly, specular reflective nature of the MLI causes variation in the short-wave radiance values, but of primary importance is the lack of a VIS-band signature during the eclipse (zero value) when a LWIR signature is still present. The short-wave signature relies on reflected solar illumination, meaning orbiting objects cannot be effectively detected during the eclipse period with such an optical sensor. In contrast, the thermal infrared signature is dominated by surface temperatures, and while shadow-induced cooling occurs, the LWIR signature remains observable. This suggests that a multi-spectral approach for the remote sensing of RSOs could be valuable for some observation missions, combining the strengths of both emissive and reflective wavebands.

During the eclipse, all components cool; see Figure 13 for temperatures and Figure 14 for the subsequent LWIR signatures. The non-PV active components cool at approximately the same rate for the “ON” and “OFF” satellites, but the PV panels are again a bit of an exception. The eclipse-induced cooling seen in the temperature plot dominates the LWIR signature of the satellite, due to the percentage of pixels on target that observe the PV array. Once the eclipse ends and sunlit again illuminates the underside of the satellite, the temperatures (and LWIR radiance averages) increase.

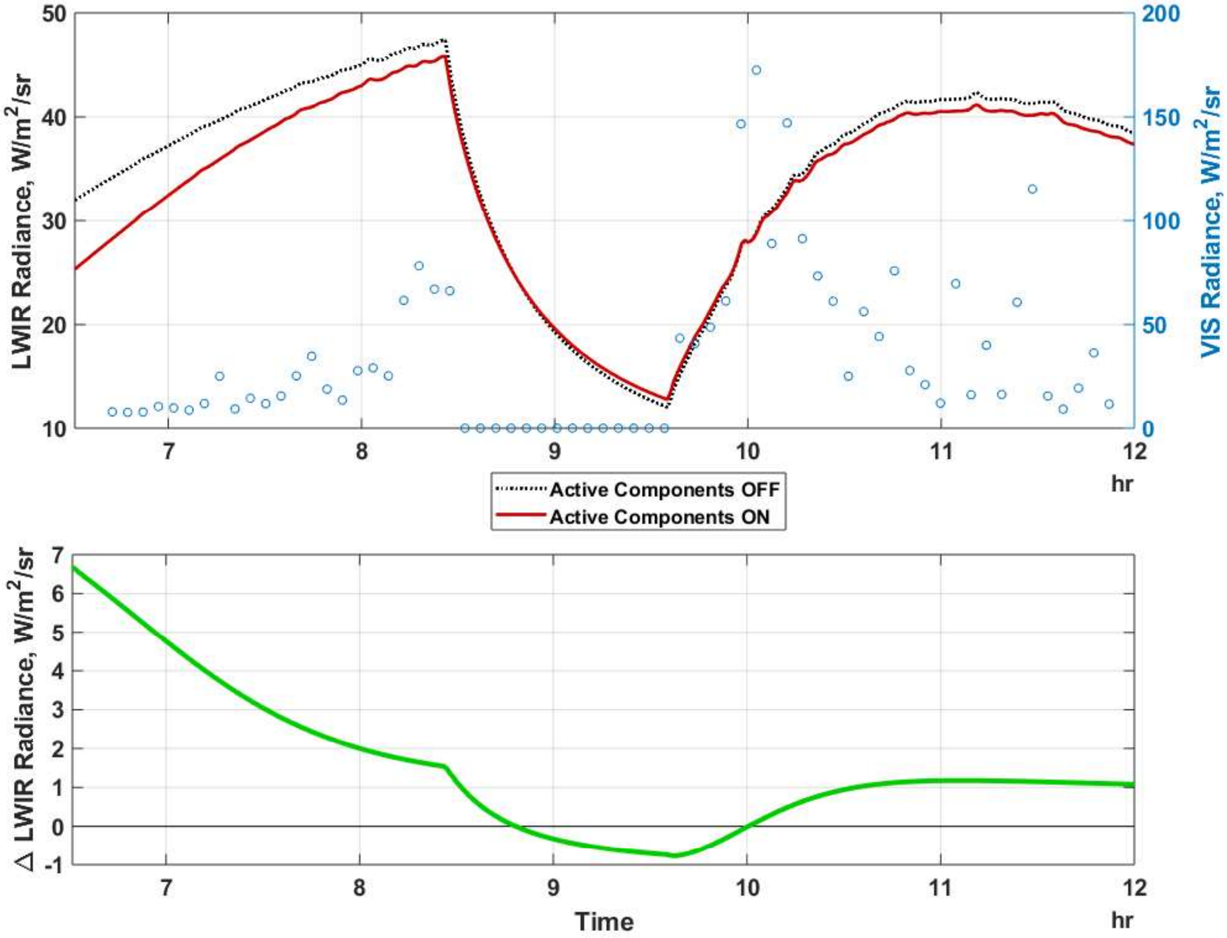

Fig. 14: Multi-spectral radiance results for a communications satellite in GEO where the average satellite signature, from the perspective of an Earth-based telescope, is shown for two power states. The average LWIR signature is shown on the primary (left) Y-axis for both the “OFF” and “ON” satellites (dotted black and thick red, respectively) as a function of time in the upper subplot. The VIS-band signature, plotted on the right Y-axis, is shown with open blue circles for reference. The lower subplot depicts (in green) the transient LWIR radiance delta between the two satellite models.

The difference between the "OFF" and "ON" satellite signatures is portrayed in the lower (green) subplot of Figure 14. Positive values indicate time periods when the deactivated satellite is warmer (on average) than the active satellite, and negative values depict times when the "ON" satellite has a higher LWIR signature than the "OFF" model. Figure 15 presents MuSES-predicted (well-resolved) LWIR sensor radiance images for the two satellite operational states ("ON" and "OFF") for two orbit positions (sunlit and eclipsed, 06:31 and 09:30, respectively). These radiance images show the while the active components on the Earth-facing exterior side of the central bus (e.g., antennas) are warmer when the satellite is operations, the inactive PV panels of the "OFF" satellite are warmer (especially during sunlit times) due to lack of solar energy conversion.

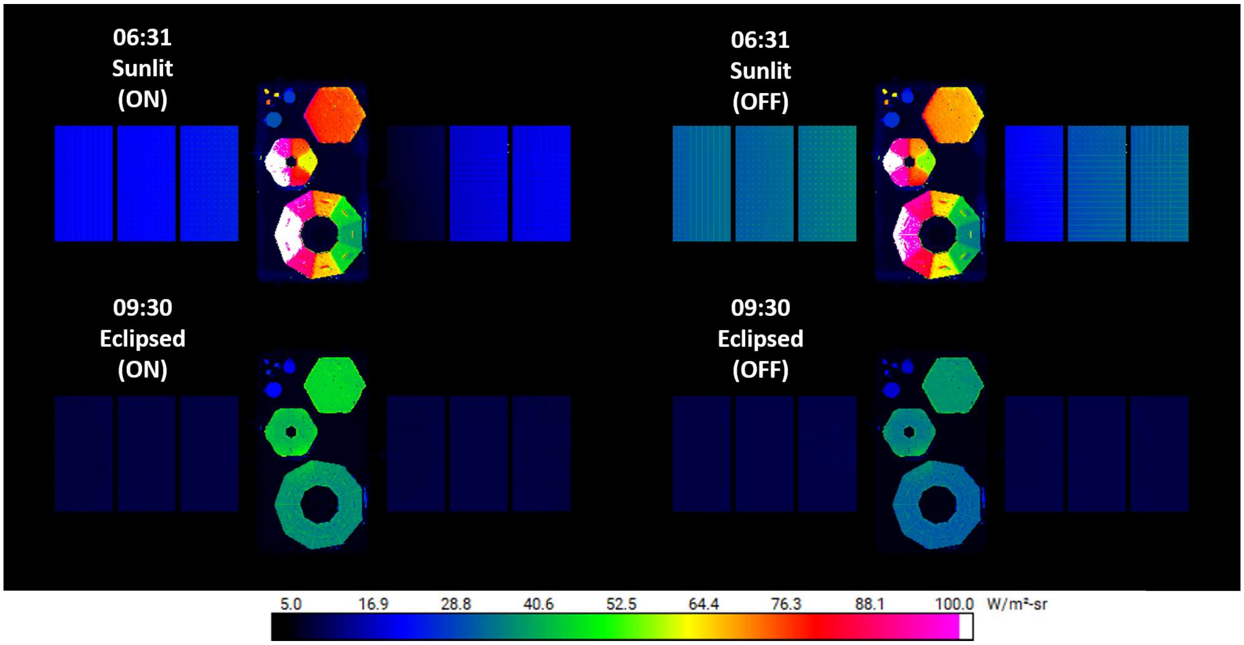

Fig. 15: MuSES-generated LWIR radiance imagery for "ON" and "OFF" communications satellites in GEO, shown at two times during the orbit. The left and right columns compare the two operations states, while the top and bottom rows contrast the sunlit (06:31) and eclipsed (09:30) orbit positions.

4.3 Distinguishing Between Satellite Operational States in GOES-17 GEO

To demonstrate the observability of the signal difference between the two operational states, we make use of "typical" sky background radiance data from Cerro Paranal [11]. To simplify atmospheric transmission effects, we consider multiple 1 μm waveband segments across the 8-12 μm astronomical N band. We used data for the highest value of precipitable water vapor shown in Fig. 1 of [11], implying the highest sky temperature (see Fig. 2 of [11]). Note that the Cerro Paranal summit is at an elevation of 8,645 feet, well below the AMOS site.

To obtain the flux (in photons/sec) emitted by the communications satellite and then collected by a ground-based telescope aperture, we integrated MuSES-predicted hyperspectral radiance values (given in W m^{-2} sr$^{-1}\mu$m^{-1}) to calculate band-integrated radiances (given in W m^{-2} sr^{-1}) for all the satellite-radiating pixels in highly-resolved sensor radiance images. These band-integrated radiance results are multiplied by the total area of the virtual sensor pixels projected onto the target and the solid angle of the AEOS-inspired ground aperture as seen from the object's GEO orbit. We then divide the resulting power (in Watts) by hc/λ to obtain photon fluxes. These fluxes, given in photons/sec for the AEOS aperture, are shown in Fig. 16 for the two satellite operational states.

To obtain the sky background flux in photons/sec for the telescope aperture of interest, we multiply the sky background radiance (in W m^{-2} sq-arcsec^{-1} μm^{-1}) by the AEOS aperture area, the wavelength interval, and the square of the FOV, again dividing by hc/λ. Assuming the dominant noise source is shot noise fluctuations from the signal and sky background, the "difference signal SNR" (dSNR) can be defined as

$$\mathrm{dSNR} = \frac{S_1 - S_0}{\sqrt{S_1 + S_0 + B}} \tag{1}$$

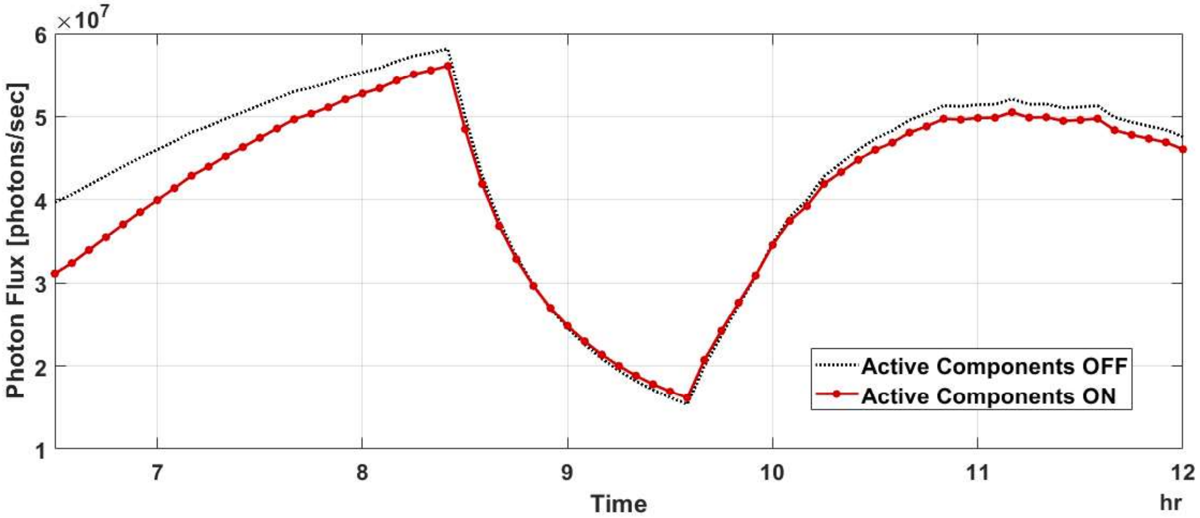

Fig. 16: Signal levels, given in photons/sec, for the two previously-described satellite operational states.

where S_1 is the signal from the satellite in its active "On" state, S_0 is the signal from the "Off" state, and B is the sky background. Using the correct FOV and the AEOS aperture area, we plot dSNR in Fig. 17 for an integration time of one second.

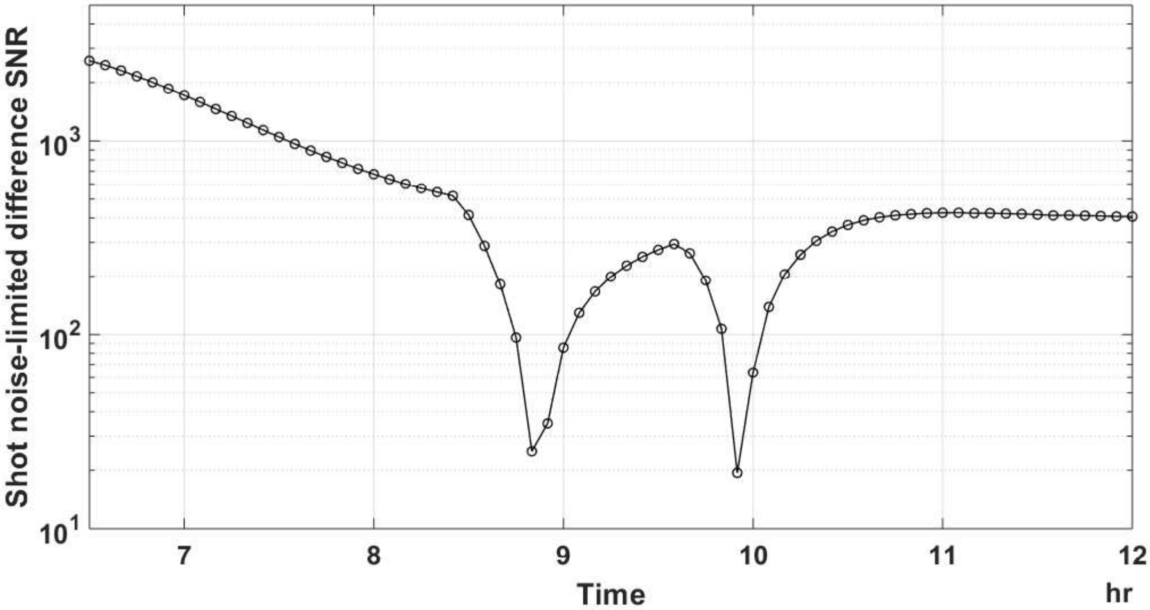

Fig. 17: Difference SNR (dSNR) for the two communications satellite operational states, assuming an integration time of one second.

The calculated difference in signal levels for the two satellite states seems to be observable, if an "above the noise" dSNR is defined as dSNR > 1. These results show that changes in operational state can likely be observed using meter-class telescopes and practical integration times. Given a viable forward model, such as we have demonstrated here with MuSES, such observations may be used to estimate RSO state or changes in state from prediction data.

5. CONCLUSION

We have demonstrated the capability of using the commercial thermal and EO/IR software MuSES™ for predicting surface temperatures of a communications satellite, in both LEO and GEO orbits, for two operational states ("On" and "Off"). As we showed, by automatically coupling thermal and electrical solvers in a single dynamic simulation process, temperature- and solar angle-dependent PV panel efficiency was calculated and used to predict the amount of harvested solar energy. This solar energy is used to power the electronic load of an orbiting communications satellite, with excess energy being used to charge the multi-cell battery pack. The battery pack, which charges when excess sunlight is present, discharges as necessary when the available PV-captured energy is insufficient for operational needs (such as during an eclipse). This coupled thermal-electrical MuSES simulation process yields predictions of battery temperature, battery charge status (and even battery lifetime, if desired), solar panel temperatures and the temperature of all elements in the 3D model. Combined with spectral optical surface properties, EO/IR radiance predictions can be made by MuSES for a wide spectrum of band-integrated and hyperspectral sensors. While LWIR renderings are the focus of this work, MWIR and VIS-band results were also shown, demonstrating the wide spectrum of EO/IR possibilities. Additionally, temperature results (stored in the MuSES TDF file format) can be read by other simulation packages when desired/necessary.

In this work, multi-spectral light curves were generated in visible, SWIR and LWIR bands and incorporated battery cells, PV panels, multi-layer insulation (MLI) blankets and both interior and exterior electronics. Our results show that, during eclipse periods, the radiance in the solar-dependent (shortwave) spectral bands falls off. In contrast, the LWIR radiance values remain significant even during shadowed orbit segments, representing an observable thermal infrared signature during these times. However, these LWIR signatures are temperature-dependent and thus decrease as the temperatures of a communications satellite oscillates.

Future work will include the addition of passive and active thermal management components and other internal sources that may contribute to the overall thermal signature of an orbiting satellite. For example, MuSES can automatically activate heating elements (e.g., battery heaters) to keep sensitive components at stable temperatures inside a desired range of operating conditions in the absence of solar heating. In addition, other components such as thrusters, heat pipes, deployable radiators, sun-tracking PV panels and phase-change materials (PCM) can be included.

6. ACKNOWLEDGEMENTS

The authors thank Eric Marttila, Derrick Levanen, Tim Viola, Jacob Hendrickson and Luke Marttila of ThermoAnalytics for their assistance during the early stages of this effort. We also thank David Witte, associated with the AFRL, for his helpful comments on our 2023 AMOS paper which lead to valuable improvements in our methodology and resulting paper this year.

7. REFERENCES

[1] Katelyn Elizabeth Boushon. *Thermal analysis and control of small satellites in low Earth orbit*. Missouri University of Science and Technology, 2018.

[2] Robert Crow, Kathy Crow, Richard Preston, and Elizabeth Beecher. Hyperspectral measurements of space objects with a small format sensor system. In *Advanced Maui Optical and Space Surveillance (AMOS) Technologies Conference*, page 61, 2017.

[3] Casey Demars, Corey D. Packard, David W. Tyler, and Christopher Rodgers. High-fidelity simulation of dynamic thermal satellite signatures with muses. In *Advanced Maui Optical and Space Surveillance Technologies Conference (AMOS)*, 2023.

[4] Ahmed Elhefnawy, Ali Elmaihy, and Ahmed Elweteedy. Passive thermal control design and analysis of a university-class satellite. *Journal of Thermal Analysis and Calorimetry*, 147(23):13633–13651, 2022.

[5] Emanuel Escobar, Marcos Diaz, and Juan Cristóbal Zagal. Evolutionary design of a satellite thermal control system: Real experiments for a cubesat mission. *Applied Thermal Engineering*, 105:490–500, 2016.

[6] Alejandro Garzón and Yovani A Villanueva. Thermal analysis of satellite Libertad 2: A guide to CubeSat temperature prediction. *Journal of Aerospace Technology and Management*, 10:e4918, 2018.

[7] Timofey Golubev and Richard R Lunt. Evaluating the electricity production of electric vehicle-integrated photovoltaics via a coupled modeling approach. In *2021 IEEE 48th Photovoltaic Specialists Conference (PVSC)*, pages 0155–0159. IEEE, 2021.

[8] Doyle Hall, John Africano, David Archambeault, Brian Birge, David Witte, and Paul Kervin. Amos observations of nasa's image satellite. In *The 2006 AMOS Technical Conference Proceedings*, pages 10–14, 2006.

[9] Doyle Hall, Paul Kervin, Andrew Nicholas, Jake Griffiths, Ivan Galysh, and Michael Werth. Multi-sensor observations of the spinsat satellite. In *Advanced Maui Optical and Space Surveillance Technologies Conference*, page 66, 2015.

[10] Derek Hengeveld and Jacob Moulton. Automatic creation of reduced-order models using Thermal Desktop. 48th International Conference on Environmental Systems, 2018.

[11] Ronald Holzlöhner, Stefan Kimeswenger, Wolfgang Kausch, and Stefan Noll. Bolometric night sky temperature and subcooling of telescope structures. *Astronomy & Astrophysics*, 645:A32, 2021.

[12] M. Klein, P. Rynes, A. Ifarraguerri, T. Anderson, and G. Whittier. Validation of a MWIR and LWIR MuSES signature model of a camouflage net. In *Proc. of the MSS Specialty Group on Battlefield Survivability and Discrimination*. SENSIAC, GTARC, Atlanta, GA, 2012.

[13] Corey Packard, Timofey Golubev, Daniel Woodford, Madison Rosiek, and Zachary Edel. Small satellite validation of a simulation approach for assessing dynamic temperatures in orbit. In *52nd International Conference on Environmental Systems (ICES)*, 2023.

[14] Scott Peck, Theodore Olszanski, Sonya Zanardelli, and Matt Pierce. Validation of a thermal-electric li-ion battery model. *SAE International Journal of Passenger Cars-Electronic and Electrical Systems*, 5(2012-01-0332):154–163, 2012.

[15] Scott Peck and Matt Pierce. Development of a temperature-dependent li-ion battery thermal model. Technical report, SAE Technical Paper, 2012.

[16] Scott Peck, Aditya Velivelli, and Wilko Jansen. Options for coupled thermal-electric modeling of battery cells and packs. *SAE International Journal of Passenger Cars-Electronic and Electrical Systems*, 7(2014-01-1834):273–284, 2014.

[17] P. Rynes, M. Klein, C. Packard, D. Less, T. Viola, and P. Capuzzi. A model-based system to evaluate the EOIR signature of special operations forces. In *Proc. of the MSS Specialty Group on Battlefield Survivability and Discrimination*. SENSIAC, GTARC, Atlanta, GA, 2014.

[18] Kameron Simon, Steve Williams, and Ian Hersom. Passive RF in support of LEO orbit determination. In *2022 Advanced Maui Optical and Space Surveillance Technologies Conference (AMOS)*, 2022.

[19] David W Tyler and Casey Demars. Airlight-imposed errors for space-object polarimetric observations from the ground. *Applied Optics*, 57(9):2235–2244, 2018.

[20] David Vallado, Paul Crawford, Richard Hujsak, and TS Kelso. Revisiting spacetrack report# 3. In *AIAA/AAS Astrodynamics Specialist Conference and Exhibit*, page 6753, 2006.

[21] Michael L Vigil, David J Witte, Paul D LeVan, Patricia J Wallentine, David E Briscoe, and Danny L Anderson. Sensor suite for the advanced electro-optical system (aeos) 3.6-m telescope. In *Imaging spectrometry II*, volume 2819, pages 151–169. SPIE, 1996.

[22] Michael Werth, Brandoch Calef, Daniel Thompson, and Lisa Thompson. Fusing lwir data and visible imagery with multi-frame blind deconvolution. In *2016 IEEE Aerospace Conference*, pages 1–10. IEEE, 2016.

[23] Charles J Wetterer and Moriba Jah. Attitude determination from light curves. *Journal of Guidance, Control, and Dynamics*, 32(5):1648–1651, 2009.